The imprint of dark matter haloes on the size and velocity dispersion evolution of early-type galaxies

Lorenzo Posti,[1,2]★ Carlo Nipoti,[1] Massimo Stiavelli[2] and Luca Ciotti[1]

[1]*Dipartimento di Fisica e Astronomia, Università di Bologna, viale Berti-Pichat 6/2, I-40127 Bologna, Italy*
[2]*Space Telescope Science Institute, 3700 San Martin Drive, Baltimore, MD 21218, USA*

ABSTRACT

Early-type galaxies (ETGs) are observed to be more compact, on average, at $z \gtrsim 2$ than at $z \simeq 0$, at fixed stellar mass. Recent observational works suggest that such size evolution could reflect the similar evolution of the host dark matter halo density as a function of the time of galaxy quenching. We explore this hypothesis by studying the distribution of halo central velocity dispersion (σ_0) and half-mass radius ($r_{\rm h}$) as functions of halo mass M and redshift z, in a cosmological Λ cold dark matter N-body simulation. In the range $0 \lesssim z \lesssim 2.5$, we find $\sigma_0 \propto M^{0.31-0.37}$ and $r_{\rm h} \propto M^{0.28-0.32}$, close to the values expected for homologous virialized systems. At fixed M in the range $10^{11}\,{\rm M}_\odot \lesssim M \lesssim 5.5 \times 10^{14}\,{\rm M}_\odot$ we find $\sigma_0 \propto (1+z)^{0.35}$ and $r_{\rm h} \propto (1+z)^{-0.7}$. We show that such evolution of the halo scaling laws is driven by individual haloes growing in mass following the evolutionary tracks $\sigma_0 \propto M^{0.2}$ and $r_{\rm h} \propto M^{0.6}$, consistent with simple dissipationless merging models in which the encounter orbital energy is accounted for. We compare the N-body data with ETGs observed at $0 \lesssim z \lesssim 3$ by populating the haloes with a stellar component under simple but justified assumptions: the resulting galaxies evolve consistently with the observed ETGs up to $z \simeq 2$, but the model has difficulty in reproducing the fast evolution observed at $z \gtrsim 2$. We conclude that a substantial fraction of the size evolution of ETGs can be ascribed to a systematic dependence on redshift of the dark matter haloes structural properties.

Key words: galaxies: evolution – galaxies: formation – galaxies: haloes – dark matter.

1 INTRODUCTION

Since early studies in the 1970s, we know that early-type galaxies (ETGs) adhere to some empirical scaling relations, such as the luminosity–velocity dispersion (Faber & Jackson 1976), size–surface brightness (Kormendy 1977), Fundamental Plane (Djorgovski & Davis 1987; Dressler et al. 1987), black hole mass–bulge mass (Magorrian et al. 1998), black hole mass–velocity dispersion (Ferrarese & Merritt 2000; Gebhardt et al. 2000) and black hole mass–Sérsic index (Graham et al. 2001; Graham & Driver 2007) relations. Such correlations, some of which were first used as distance estimators to help building the distance scale ladder, have given the astrophysical community important clues about the possible scenarios of galaxy formation (e.g. Ciotti 2009). In this respect, the stellar mass–size relation has currently a special role, because galaxy sizes and masses can be measured out to $z \simeq 2.5$–3. With such data available, different authors found indications that the population of ETGs undergoes a significant size evolution from

$z \simeq 3$ to 0, such that present-day galaxies have, on average, significantly larger sizes than higher-z galaxies of similar stellar mass (see e.g. Stiavelli et al. 1999; Ferguson et al. 2004; Daddi et al. 2005; Trujillo et al. 2006; Cimatti et al. 2008; van der Wel et al. 2008; van Dokkum et al. 2008; Saracco, Longhetti & Andreon 2009; Cassata et al. 2011; Damjanov et al. 2011; Krogager et al. 2013). For the current galaxy formation models it is still challenging and non-trivial to explain such behaviour of massive ETGs. Various mechanisms have been proposed to explain the observed size evolution, including dry (i.e. dissipationless) major and minor merging (see Khochfar & Silk 2006; Hopkins et al. 2009b; Naab, Johansson & Ostriker 2009; Nipoti et al. 2009b; López-Sanjuan et al. 2012; Laporte et al. 2013; Sonnenfeld, Nipoti & Treu 2014) and feedback-driven expansion (see e.g. Fan et al. 2008, 2010; Ragone-Figueroa & Granato 2011; Ishibashi, Fabian & Canning 2013). Currently, the issue is far from being resolved and further observations, together with more comprehensive theoretical models, are desirable.

Recently, Carollo et al. (2013, see also Poggianti et al. 2013) argued that the median size growth of ETGs of stellar mass $10^{10.5}\,{\rm M}_\odot \leq M_* \leq 10^{11}\,{\rm M}_\odot$ could be due to the dilution of the sample of galaxies quenched at early times in a population of bluer

★ E-mail: lorenzo.posti@unibo.it

and larger galaxies that have been quenched much later. In the sample of ETGs with $M_* > 10^{11}$ M$_\odot$ the same authors find indications of intrinsic size evolution, which cannot be explained with the dilution of the population. In other words, Carollo et al. (2013) find evidence that not all the progenitors of local quenched-ETGs can be identified with the compact quiescent ETGs observed at $z \simeq 1$–2, because a substantial fraction of present-day ETGs have stopped forming stars much later than the higher-z ETGs. An interesting conclusion of Carollo et al. (2013) is that the stellar density of ETGs scales with the mean density of the Universe *at the time of quenching*. This suggests that the host halo evolution could be the main driver of the galaxy evolution, in the sense that the redshift dependence of the properties of an ETG results similar to that of its host halo (see also recent results by Stringer et al. 2013).

The natural tool to explore such halo-galaxy connection would be a large-scale, high-resolution, cosmological simulation jointly following the evolution of dark matter (hereafter DM) and baryons, including star formation and feedback. However, given the well-known uncertainties and technical issues still present in this method (see e.g. Kereš et al. 2012; Vogelsberger et al. 2012; Hopkins, Narayanan & Murray 2013), we adopt here a simpler approach, trying to extract useful information on the evolution of ETGs studying the behaviour of a population of DM haloes in a DM-only cosmological simulation. We focus our attention on the scaling laws of DM haloes in a Λ cold dark matter (ΛCDM) Universe and in particular on their size and velocity dispersion evolution. Our aim is trying to understand whether the evolution of the haloes is somehow similar to that of ETGs which are expected to be hosted in such haloes. Therefore, we will also try to compare our N-body data with available observations of ETGs, populating haloes with galaxies under simple but justified assumptions.

This paper is organized as follows: in Section 2 we present the methods of our investigation and we set the stage with all the definitions and simple theoretical expectations; in Section 3 we show our results on the scaling relations of the dark halo population; in Section 4 we trace the merger histories of individual haloes which are representative for the entire population; in Section 5 we link the dark halo properties with those of the ETGs and compare the predicted size and velocity dispersion evolution with recent observations; Section 6 summarizes and concludes.

2 METHODS AND DEFINITIONS

2.1 Computational tools

We performed a cosmological N-body simulation with the publicly available code GADGET-2 (Springel 2005, see also Springel, Yoshida & White 2001) in a standard ΛCDM flat Universe where the matter density, dark energy density and Hubble constant are, respectively, $\Omega_{0,m} = 0.28$, $\Omega_{0,\Lambda} = 0.72$ and $H_0 = 70$ km s^{-1} Mpc^{-1}. In the run we simulated the evolution of $512^3 \simeq 1.3 \times 10^8$ particles of mass $M_{part} \simeq 1.5 \times 10^9$ M$_\odot$ h^{-1}, from $z = 99$ to 0, in a cosmological comoving box of side $l = 128$ Mpc h^{-1}, where h is the reduced Hubble constant $h = H_0/100$ km s^{-1} Mpc^{-1}. The initial conditions of the simulation were generated using a modified version of the publicly available code GRAFIC2 (see Bertschinger 2001). We used a softening length of $\sim$1 kpc h^{-1} throughout the simulation. The simulation was run on 72 cores on the UDF Linux cluster at the Space Telescope Science Institute (Baltimore, MD) and took about 6 d to complete. We produced 16 snapshots equally spaced in log a, where $a(t) = (1 + z)^{-1}$ is the cosmic scale factor, from $z \simeq 2.5$ to 0.

2.2 Definitions of the structural and kinematical properties of dark matter haloes

In this section, we define the fundamental structural and kinematical properties of the simulated DM haloes, such as the mass M, the size r and the velocity dispersion σ. There is not a unique method to identify a DM halo in a cosmological N-body simulation, because, as for every non-truncated and non-isolated particle system, it is not trivial to define the set of particles that belong to the object: various techniques have been proposed in the astrophysical literature (e.g. friends-of-friends or spherical overdensity algorithms;[1] see Davis et al. 1985; Efstathiou et al. 1985; Lacey & Cole 1993; Evrard et al. 2008). The problem is relevant, because different sets of particles can lead to different estimates of the properties of the object.

In this work, we adopted the conventions of Knollmann & Knebe (2009) and we have used their AHF finding code. The haloes are identified from the peaks of a three-dimensional density field calculated in a grid with adaptive mesh refinement (AMR). The spherical region of radius r_Δ, which is centred at the centre of mass of the particles in the highest refinement level of the AMR grid, defines the set of particles that belong to the DM halo[2] (see Knollmann & Knebe 2009). We use a standard definition of a halo as a certain spherical top-hat overdensity, via the formula

$$\frac{3M}{4\pi r_\Delta^3} = \Delta_c(z)\rho_c(z), \tag{1}$$

where $\rho_c(z) = 3H^2(z)/8\pi G$ is the critical density of the Universe at redshift z, $\Delta_c(z)$ is the overdensity value at the same time, $H(z)$ is the Hubble parameter and G is the gravitational constant. We adopt the following definition of the critical overdensity in a flat Universe with negligible radiation energy density:

$$\Delta_c(z) = 18\pi^2 + 82[\Omega(z) - 1] - 39[\Omega(z) - 1]^2, \tag{2}$$

where $\Omega(z) = \Omega_{0,m}(1+z)^3/E(z)^2$ and $E(z)^2 = \Omega_{0,m}(1+z)^3 + \Omega_{0,\Lambda}$, such that the haloes identified are expected to be close to equilibrium (see Lacey & Cole 1993; Bryan & Norman 1998).

Given the velocities of all particles belonging to the halo, we compute the *virial* velocity dispersion of the system

$$\sigma_V = \left[\sum_{i=1}^{N} \sum_{j=1}^{3} \frac{(v_{i,j} - \bar{v}_j)^2}{N} \right]^{1/2}, \tag{3}$$

where N is the number of particles in the halo, $v_{i,j}$ is the jth component of the ith particle's velocity and $\bar{v}_j$ is the jth component of the average velocity.

The definition of the halo size is also non-trivial, since it is intimately affected by the choice of the spherical overdensity. As a matter of fact the definition of r_Δ via equation (1) is based on the idea that the material surrounding the overdensity is bound to the halo if the dynamical time of the particle is less than the Hubble time at that redshift, so one can reasonably expect the halo of size r_Δ to be in equilibrium. For this reason, r_Δ is often, but improperly, called *virial radius* and, in any case, in the following we will adopt such convention. However, other definitions of the halo

---

[1] For a brief review of different methods see Knebe et al. (2011).
[2] An *unbinding procedure* is also run on the haloes in order to remove the gravitationally unbound particles inside the spherical region (see Knollmann & Knebe 2009).

size are possible: for example, the gravitational radius (i.e. the true virial radius)

$$r_{\rm g} \equiv \frac{GM}{\sigma_{\rm V}^2} \qquad (4)$$

and the half-mass radius $r_{\rm h}$, i.e. the radius of the sphere enclosing half the total mass of the halo, $M(<r_{\rm h}) = M/2$.

We also employ a definition of the halo velocity dispersion alternative to $\sigma_{\rm V}$: we compute the velocity dispersion profile $\sigma(<r)$ in the same fashion as the mass profile, where the velocity dispersion is calculated as in equation (3) and the sum is only on the particles within the spherical region of radius r. From the $\sigma(<r)$ profile, we then estimate the *central velocity dispersion*

$$\sigma_0 \equiv \sigma(<r_{\rm h}). \qquad (5)$$

We define our sample of DM haloes by selecting those for which $r_{\rm h} > 2r_{\rm conv}$, where $r_{\rm conv}$ is the convergence radius in the sense of Power et al. (2003), i.e. the radius within which the two-body collisions dominate the orbital motions of the particles integrated by the code and the density estimates are therefore unreliable. We verified that, for our sample, the mass contained within the convergence radius is typically a small fraction of that contained within the half-mass radius, so our measurement of σ_0 should be robust. The sample selected with the above criterion is made of $\approx 11\,000$ DM haloes, with a lower limit in mass $M_{\rm lower} \simeq 1.3 \times 10^{11}\,{\rm M_\odot}$.

2.3 Behaviour of the different size and velocity dispersion proxies

In this section we discuss the relations between different size and velocity dispersion estimators, in particular how the *virial* proxies (r_Δ, $\sigma_{\rm V}$) compare to the *central* ones ($r_{\rm h}$, σ_0).

In this work we use σ_0 and $r_{\rm h}$ (see Section 2.2) to characterize the haloes because it is reasonable to expect that the stellar central velocity dispersion σ_* and the effective radius $R_{\rm e}$ of the galaxies inside such haloes are more related to the halo central quantities than to the halo virial quantities. However, different choices would be possible. For instance, a tight correlation between r_Δ and $R_{\rm e}$ has been suggested, both theoretically (see Mo, Mao & White 1998) and using abundance matching techniques (see Kravtsov 2013). In addition, it is well known that the ratio $r_{\rm g}/r_{\rm h}$ depends only weakly on the density profile (see Ciotti 1991; Nipoti, Londrillo & Ciotti 2003; Binney & Tremaine 2008). It is therefore interesting to verify how the different proxies correlate in our sample of haloes and how their values depend on the choice of the critical overdensity $\Delta_{\rm c}$.

In Fig. 1 we show the dependence of r_Δ, $r_{\rm g}$ and $r_{\rm h}$ on $\Delta_{\rm c}$ at $z = 0$ for a representative halo with $M \simeq 10^{13}\,{\rm M_\odot}$. As expected from equation (1), the virial radius has a perfect $r_\Delta \propto \Delta_{\rm c}^{-1/3}$ scaling. We note that also the gravitational radius scales roughly as $r_{\rm g} \propto \Delta_{\rm c}^{-1/3}$ and this is because it depends only on virial quantities (see equation 4), while the half-mass radius has slightly less steep dependence on $\Delta_{\rm c}$, namely $r_{\rm h} \propto \Delta_{\rm c}^{-0.22}$. This is an additional reason to prefer $r_{\rm h}$ to r_Δ in the present context. Formally, also the quantity $\sigma_{\rm V}$, and so σ_0, depends on $\Delta_{\rm c}$, but the dependence is weak: the variation is no more than 10 per cent in $\sigma_{\rm V}$, when varying $\Delta_{\rm c}$ by an order of magnitude.

In Fig. 2 we show the distributions of the halo population at $z = 0$ in the $\sigma_0 - \sigma_{\rm V}$, $r_{\rm h} - r_\Delta$ and $r_{\rm g} - r_\Delta$ planes. We find that in all cases a linear correlation is in good agreement with the distribution of the haloes in the three planes; fitting with power laws we get $\sigma_0 \propto \sigma_{\rm V}^{0.97 \pm 0.01}$, $r_{\rm h} \propto r_\Delta^{0.96 \pm 0.01}$ and $r_{\rm g} \propto r_\Delta^{1.1 \pm 0.01}$. Interestingly, for a given halo, the ratio $\sigma_0/\sigma_{\rm V}$ is very close to unity: the average
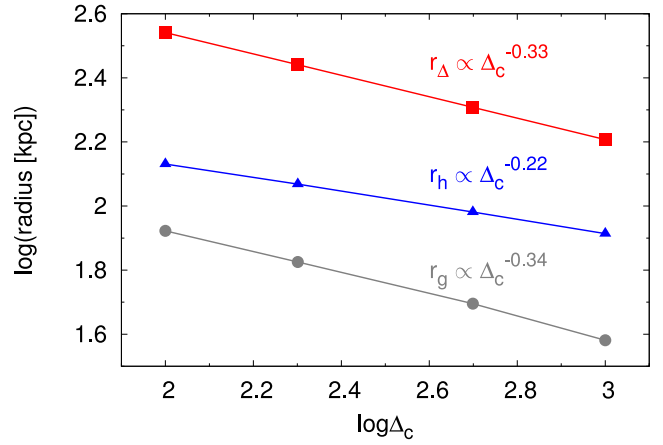

Figure 1. Virial radius (red squares, see equation 1), gravitational radius (grey circles, see equation 4) and half-mass radius (blue triangles) as functions of the critical overdensity $\Delta_{\rm c}$ for a $M \simeq 10^{13}\,{\rm M_\odot}$ halo, taken from the $z = 0$ snapshot of the simulation.

ratio in our sample is $\langle \sigma_0/\sigma_{\rm V} \rangle = 1.01$. We recall that it is not a priori expected that the central quantities correlate linearly with the virial ones. This finding indicates that the DM haloes are not systematically non-homologous: in other words, more massive haloes are, on average, just rescaled versions of less massive haloes (at least, as far as the relation between virial and central quantities is concerned). The scatter around the linear relations in Fig. 2 can be ascribed to some degree of non-homology at a given halo mass or to the fact that some haloes are not completely virialized. We note also that Diemer, Kravtsov & More (2013b) recently found that there is a remarkable homology in their cluster-sized haloes sample: they argued that a tight relation exists between the mass and velocity dispersion profiles of DM haloes. Moreover, they claimed that the mass–velocity dispersion relation of the halo sample is almost insensitive to the size definition (in the range $100 < \Delta_{\rm c} < 2500$ in equation 1) because of such homology in the radial profiles.

For the purposes of this work, given that, on average, the central quantities ($\sigma_0, r_{\rm h}$) scale linearly with the virial quantities ($\sigma_{\rm V}, r_\Delta$), our results would be virtually unchanged if we adopted $\sigma_{\rm V}$, instead of σ_0, and r_Δ or $r_{\rm g}$, instead of $r_{\rm h}$, to characterize our haloes.

2.4 Virial expectations for the halo mass–velocity dispersion and mass–size relations

With the adopted halo definition (equation 2) we expect the DM haloes to be virialized in every snapshot of the simulation from $z \simeq 2.5$ to 0. It follows that some well-known scaling laws are expected for the dark halo population: from equation (4), under the assumption of a linear proportionality between the virial radius (equation 1) and the gravitational radius (equation 4) it follows (e.g. Lanzoni et al. 2004) that for haloes in equilibrium

$$M \propto \sigma_{\rm V}^3. \qquad (6)$$

The correlation is expected to depend on redshift as

$$\sigma_{\rm V} \propto [E(z)\,M]^{1/3} \qquad (7)$$

(see e.g. Evrard et al. 2008). Using equation (1) to define the haloes and the definition of the critical density $\rho_{\rm c} = 3H^2/8\pi G$, for a flat Universe we get

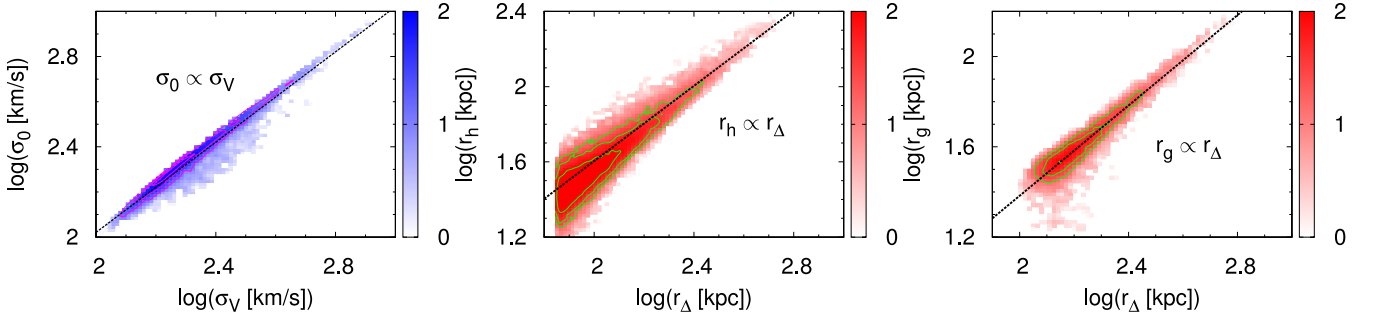$$r_\Delta = \left[2GM\,\Delta_{\rm c}(z)^{-1}\,H(z)^{-2} \right]^{1/3}, \qquad (8)$$

Figure 2. Distributions of the simulated haloes at $z = 0$ in the $\sigma_0 - \sigma_V$ (left-hand panel), $r_h - r_\Delta$ (central panel) and $r_g - r_\Delta$ (right-hand panel) planes. In each panel, the black short-dashed line is the *linear* best fit to the distribution.

where $H(z) = H_0 E(z)$. Assuming a linear dependence of the form $r_\Delta = \xi r_g$, where ξ is a dimensionless constant, then the virial velocity dispersion can be written as $\sigma_V^2 = GM\xi/r_\Delta$, implying

$$\sigma_V = \xi^{1/2} \left(\frac{GM}{\sqrt{2}} \right)^{1/3} \Delta_c(z)^{1/6} H(z)^{1/3}. \tag{9}$$

We have seen in Section 2.3 that $\sigma_0 \propto \sigma_V$, so also the mass and redshift dependence of σ_0 is expected to be given by equation (9). Under the assumption that r_h and r_g scale linearly with r_Δ (see Section 2.3), from equation (8) we have that a fixed z

$$r_h \propto r_g \propto M^{1/3}. \tag{10}$$

The z-dependence of the other size proxies is also given by equation (8), as $r_g \propto r_\Delta$ and $r_h \propto r_\Delta$ (see Section 2.3).

3 SCALING RELATIONS OF DARK MATTER HALOES AS FUNCTIONS OF REDSHIFT

Here we present the distributions of the size and the velocity dispersion as functions of mass and redshift for our sample of $\sim 11\,000$ DM haloes (see Section 2.2) in the mass range $10^{11}\,\mathrm{M}_\odot \leq M \leq 5.5 \times 10^{14}\,\mathrm{M}_\odot$. We adopt the same lower mass limit in all the snapshots of our simulation, while we do not restrict the upper mass limit, which varies from $M \simeq 2.67 \times 10^{13}\,\mathrm{M}_\odot$ at $z \simeq 2.5$ to $M \simeq 5.5 \times 10^{14}\,\mathrm{M}_\odot$ at $z = 0$.

3.1 Mass–velocity dispersion: the measured correlation and evolution

The simulated DM halo population is well represented by the following best-fitting relation:

$$\log \left(\frac{\sigma_0}{\mathrm{km/s}} \right) = \gamma \log \left(\frac{M}{\mathrm{M}_\odot} \right) + b, \tag{11}$$

where

$$\log \gamma = (0.103 \pm 0.008) \log(1 + z) - (0.49 \pm 0.002),$$

$$\log b = (0.163 \pm 0.02) \log(1 + z) + (0.179 \pm 0.006). \tag{12}$$

In Fig. 3(a) we show the distribution of the sample in the $M - \sigma_0$ plane at $z = 0$ and we find a best-fitting correlation of the type $M \propto \sigma_0^{3.04 \pm 0.01}$ (i.e. $\gamma \simeq 0.32$). For comparison we also show the best-fitting correlation at $z \simeq 2.5$: the slope is slightly larger than that at $z = 0$, i.e. $\gamma \simeq 0.37$, whereas the normalization is significantly higher: as we expected, at fixed mass higher-z haloes have higher velocity dispersion.

Assuming $\sigma_0 \propto \sigma_V$ (see Section 2.3), we can compare our results with both theoretical expectations, e.g. equation (6), and previous findings. At fixed mass $M = 10^{12}\,\mathrm{M}_\odot$ we find a good agreement with equation (7): i.e. our sample follows[3] $\sigma_{0,12} \propto E(z)^{0.36}$. In the top panel of Fig. 4 we show the evolution of the central velocity dispersion at $M = 10^{12}\,\mathrm{M}_\odot$ in the redshift range $0 \lesssim z \lesssim 2.5$. We have chosen $M = 10^{12}\,\mathrm{M}_\odot$ as a reference mass, since it is roughly the mean mass in our sample at $z = 0$ and it is still well resolved (about 8×10^2 particles). As expected from cosmological predictions (equation 7), $\sigma_{0,12}$ decreases with time. We find a power-law best-fitting evolution of the type $\sigma_{0,12} \propto (1 + z)^{0.35}$ and also a better representation (about two orders of magnitude in the reduced χ^2) of the results via the fitting formula $\log \sigma_{0,12} = 0.29\,x^2 + 0.2\,x$, where $x \equiv \log(1 + z)$. We comment here that fixing a typical mass, say $M = 10^{12}\,\mathrm{M}_\odot$ as in Fig. 4, means that we are analysing different haloes at different z, unlike fixing a halo and focusing on its evolution.

To further compare the results of our simulation with theoretical predictions and previous works, we have analysed the correlation between the mass and the virial velocity dispersion σ_V. In Fig. 3(b) we plot the distribution of the DM haloes in the $M - \sigma_V$ plane. In general, there is a very good agreement with the theoretical expectation (6) derived from the equilibrium assumption: the best-fitting relation corresponds to $M \propto \sigma_V^{2.97 \pm 0.01}$. Other authors found similar results from independent simulations (see e.g. Evrard et al. 2008; Stanek et al. 2010; Diemer et al. 2013b; Munari et al. 2013). We fitted the evolution of the normalization, at $M = 10^{12}\,\mathrm{M}_\odot$, of the $M - \sigma_V$ correlation for our simulated haloes as a function of $E(z)$. We find that from $z \simeq 2.5$ to 0 the normalization at $M = 10^{12}\,\mathrm{M}_\odot$ follows $\sigma_{V,12} \propto E(z)^{0.33}$, which is in remarkably good agreement with theoretical expectations (equation 7). We compare also our results with previous findings: for $M = 10^{14}\,\mathrm{M}_\odot$ Stanek et al. (2010) estimate an evolution $\sigma_{V,14} \propto E(z)^{0.34}$ and we find $\sigma_{V,14} \propto E(z)^{0.35}$; for $M = 10^{14.3}\,\mathrm{M}_\odot$ Lau, Nagai & Kravtsov (2010) find $\sigma_{V,14.3} \propto (1 + z)^{0.49}$ in their non-radiative case (with fixed $\Delta_c = 500$) and we find $\sigma_{V,14.3} \propto (1 + z)^{0.36}$.

3.2 Mass–size: the measured correlation and evolution

The simulated DM halo population is well represented by the following best-fitting relation:

$$\log \left(\frac{r_h}{\mathrm{kpc}} \right) = \gamma \log \left(\frac{M}{\mathrm{M}_\odot} \right) + b, \tag{13}$$

---

[3] We define $A_{X,Y} \equiv A_X(M = 10^Y\,\mathrm{M}_\odot)$.
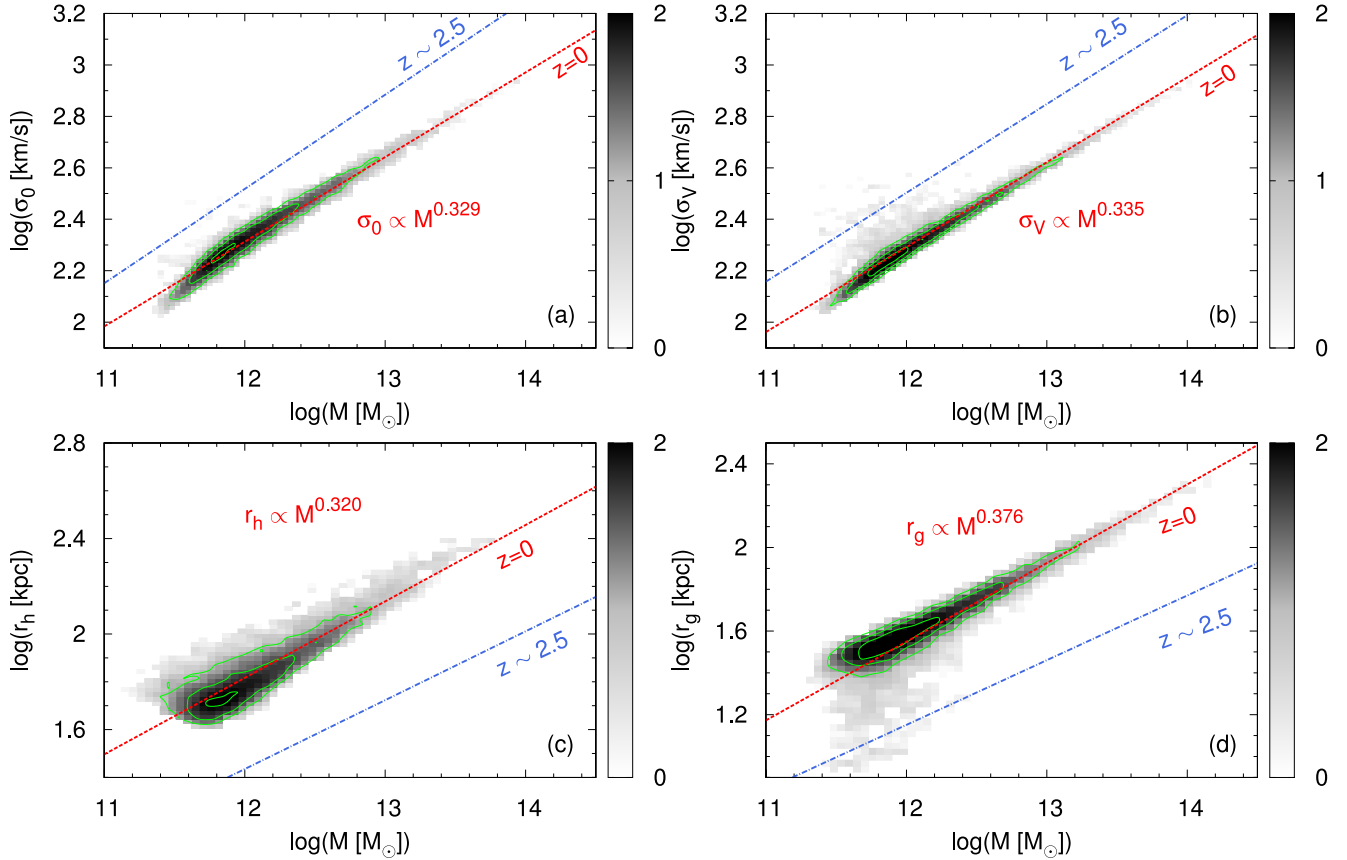
Figure 3. Distributions at $z = 0$ of the simulated haloes in the planes $M-\sigma_0$ (panel a), $M-\sigma_V$ (panel b), $M-r_h$ (panel c) and $M-r_g$ (panel d). In each panel, the plane has been binned in cells and the grey-scale represents the logarithm of the counts of haloes in each cell. The red dotted lines are the best fits at $z = 0$ ($\sigma_0 \propto M^{0.329}$, $\sigma_V \propto M^{0.335}$, $r_h \propto M^{0.320}$ and $r_g \propto M^{0.376}$); for comparison, the best fits at $z \simeq 2.5$ are plotted as blue dot–dashed lines.

where

$$\log \gamma = (-0.069 \pm 0.01) \log(1 + z) + (-0.489 \pm 0.003),$$

$$\log b = (0.02 \pm 0.02) \log(1 + z) + (0.312 \pm 0.004). \quad (14)$$

The measured correlation for the simulated haloes is shown in Fig. 3(c). The best-fitting relation computed for this sample at $z = 0$ is $M \propto r_h^{3.12 \pm 0.02}$ (i.e. $\gamma \simeq 0.32$). For comparison, we also plot here the $z \simeq 2.5$ best-fitting correlation: the slope is slightly decreasing with redshift, down to $\gamma \simeq 0.28$ and the normalization in this mass range gets lower at later times. As we expected, at fixed mass higher-z haloes have smaller size, i.e. they have higher density.

We then fit the evolution of the normalization at $M = 10^{12} \, \mathrm{M_\odot}$ of the $M-r_h$ correlation as a function of redshift in the range $0 < z < 2.5$: we find an evolution of the type $r_{h,12} \propto E(z)^{-0.65}$, which is in good agreement with the expectations given by equation (8). In the bottom panel of Fig. 4 our findings on the evolution in time of $r_{h,12}$ are shown: as expected (equation 8), we find that $r_{h,12}$ increases with time. We find a power-law best-fitting $r_{h,12} \propto (1 + z)^{-0.71}$ and also that a better representation of the results is given by $\log r_{h,12} = -0.53 x^2 - 0.41 x$, where $x \equiv \log(1 + z)$.

In Fig. 3(d) we plot the distribution of the DM haloes in the $M-r_g$ plane. Also in this case we find a reasonably good agreement with the virial expectation (10), with a best-fitting correlation $M \propto r_g^{2.71 \pm 0.02}$. We notice here that the somehow steeper slope than expected in Fig. 3(d) is due to a *tail* of the distribution composed of low-mass haloes ($M < 10^{12} \, \mathrm{M_\odot}$) with small r_g: this feature can be due to the fact that some DM haloes are not in equilibrium,

for instance, because they could have experienced a recent major merger, and so virialization is not a good assumption for such objects.

4 EVOLUTION OF INDIVIDUAL HALOES

4.1 Evolution of simulated dark haloes in the mass–velocity dispersion and mass–size planes

According to the halo definition here adopted (equation 1) the halo mass increases monotonically with time, so studying a property of a halo as a function of its mass is equivalent to studying the time evolution of the same property. Here we present the time evolution of σ_0 and r_h for some individual representative haloes in our simulation, by tracking them in the planes σ_0-M and r_h-M. In Fig. 5 we plot the evolutionary tracks followed by a representative halo with mass $M \simeq 5.5 \times 10^{14} \, \mathrm{M_\odot}$ at $z = 0$: we reconstruct the growth in velocity dispersion (top panel) and size (bottom panel) as the halo gets more massive. It is apparent that neither in the $M-\sigma_0$ nor in the $M-r_h$ plane the halo evolves along the scaling law of slope $\approx 1/3$. The actual evolution experienced by the halo in Fig. 5 is significantly shallower in the $M-\sigma_0$ plane, with best-fitting $\sigma_0 \propto M^{0.2}$, and steeper in the $M-r_h$ plane, with best-fitting $r_h \propto M^{0.6}$, consistent with the results of previous works on binary dissipationless mergers (see e.g. Nipoti et al. 2003; Boylan-Kolchin, Ma & Quataert 2005; Hopkins et al. 2009a; Hilz et al. 2012; Hilz, Naab & Ostriker 2013).
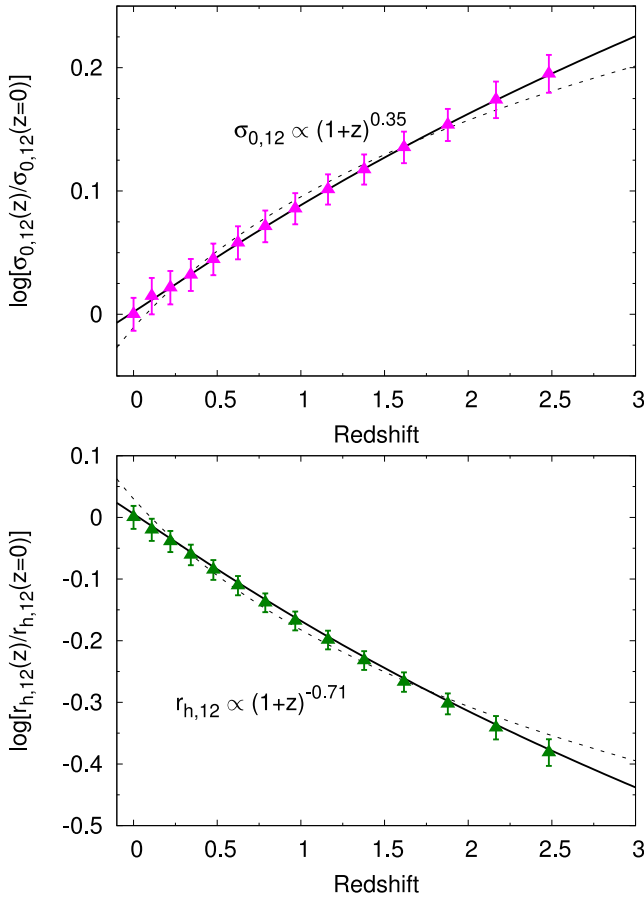
Figure 4. Top panel: halo central velocity dispersion at fixed $M = 10^{12}\,\mathrm{M}_\odot$ as a function of redshift. The black dashed line is the power-law best fit to the points, while the black solid line is a fit quadratic in logarithm (see the text). Bottom panel: same as top panel but for the half-mass radius at fixed $M = 10^{12}\,\mathrm{M}_\odot$.

Fig. 6 gives an overall picture of the evolution in the $M-\sigma_0$ (upper panel) and $M-r_\mathrm{h}$ (lower panel) planes of the whole halo population. In particular, we follow the evolution from $z \simeq 2.5$ of three objects, having $M \simeq 10^{13}$, 10^{14} and $5.5 \times 10^{14}\,\mathrm{M}_\odot$ at $z = 0$, representative of an ETG sized halo, a group sized halo and a cluster sized halo, respectively. Fig. 6 indicates that the evolutionary tracks of the whole population of DM haloes in the simulation reflect that of the halo shown in Fig. 5; therefore, we do not find clear indications of mass-dependent evolution. In other words, the velocity dispersion grows weakly and the half-mass radius grows strongly independently of the halo mass. The fact that the individual haloes experience an evolution in σ_0 with a shallower slope than the global $\sigma_0 \propto M^{1/3}$ correlation (and vice versa for the evolution in r_h) is responsible for the z-evolution of the normalization of the σ_0-M correlation, such that at fixed mass σ_0 is smaller at lower-z. Similarly, the z-evolution of the normalization of the $r_\mathrm{h}-M$ correlation is such that at fixed mass r_h is larger at lower-z.

4.2 Comparison with simple dry merger models

In a hierarchical context, the evolution and mass assembly of haloes are often decomposed in two main processes: diffuse accretion and mergers (e.g. Fakhouri, Ma & Boylan-Kolchin 2010). According to the halo definition here adopted (equation 1), the halo mass can grow in principle even in an isolated and static configuration,
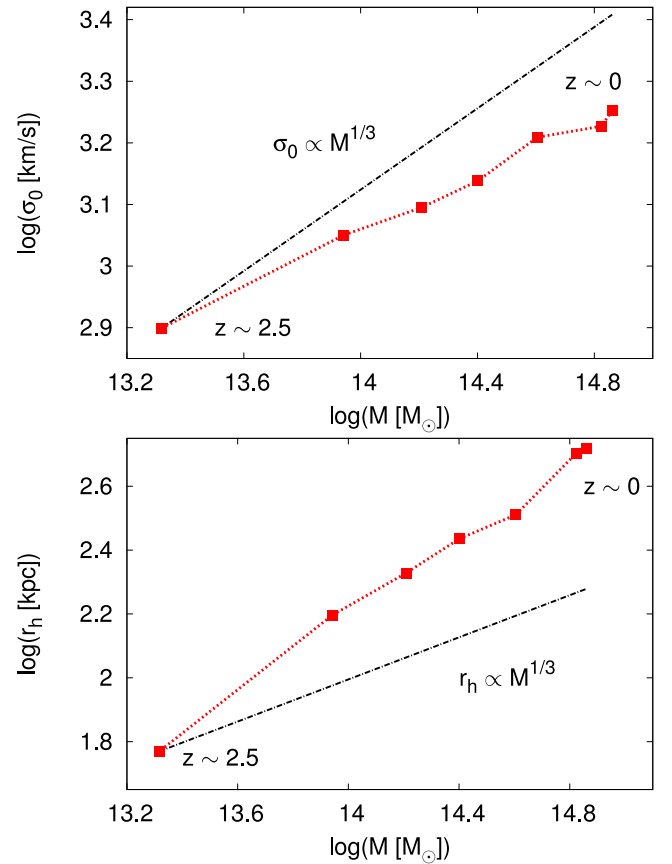

Figure 5. Top panel: evolution of a DM halo of mass $M(z = 0) \simeq 5.5 \times 10^{14}\,\mathrm{M}_\odot$ in the $M-\sigma_0$ plane from $z \simeq 2.5$ to 0 (red squares). Here, mass traces time: the least massive point is the one at highest-z. The black dot–dashed line is a power law of index $1/3$, plotted for comparison. Bottom panel: same as top panel, but in the $M-r_\mathrm{h}$ plane.

just because the critical density of the Universe decreases with time (see e.g. Diemer, More & Kravtsov 2013a). However, in a realistic cosmological context a halo experiences several mergers in its lifetime and in many cases they dominate its mass assembly. In the following, we will consider the case in which merging is the driving process for the structural evolution of individual haloes and we will compare our results with predictions of simple dry merging models.

4.2.1 Analytic arguments

Here we present some of the analytic arguments one can use to describe the evolution of the velocity dispersion and size of a halo which grows mainly via mergers with other haloes. If both the mass-loss in the collision and the orbital energy of the encounter are negligible, in an equal-mass merger scenario the halo is expected to grow in size linearly with mass, while its velocity dispersion is expected to remain constant (see e.g. Nipoti et al. 2003). Under the same hypothesis, if the evolution is dominated by accretion of many satellites much less massive than the main halo, the velocity dispersion is expected to *decrease* linearly with the mass, while the size would grow quadratically with mass (see e.g. Naab et al. 2009). In a realistic merging history consisting of both major and minor mergers, we expect the behaviour of r_h and σ_0 to be in between those predicted by the two extreme cases illustrated above.
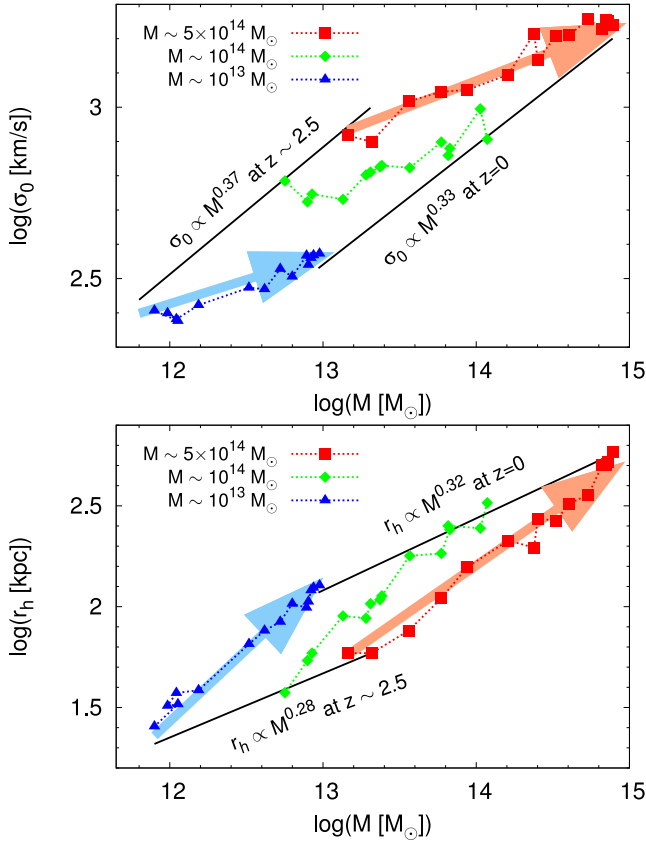
Figure 6. Top panel: evolution in the $M-\sigma_0$ plane of three representative haloes in our simulation. The red filled squares refer to a cluster-sized halo of mass $M(z=0) \simeq 5.5 \times 10^{14}\,\mathrm{M_\odot}$ (the same halo as in Fig. 5, but with a finer sampling), the green filled diamonds refer to a group-sized halo of mass $M(z=0) \simeq 10^{14}\,\mathrm{M_\odot}$, while the blue filled triangles refer to an ETG-sized halo of mass $M(z=0) \simeq 10^{13}\,\mathrm{M_\odot}$. The two black solid lines are the best-fitting $M-\sigma_0$ correlation for the whole population at $z=0$ and at $z \simeq 2.5$. The big blue and red arrows represent a schematic view of the evolutionary track in the $M-\sigma_0$ plane for, respectively, the low-mass and high-mass haloes. Bottom panel: same as top panel, but in the $M-r_h$ plane.

However, the assumptions of zero orbital energy and negligible mass-loss are not necessarily realistic. Some authors have shown how the effect of mass-loss could play an important role in the evolution of the velocity dispersion and of the size of an object (see e.g. Nipoti et al. 2003; Hilz et al. 2012). Also the effect of the orbital energy on the evolution of σ_0 and r_h can be non-negligible (Nipoti, Treu & Bolton 2009a; Nipoti et al. 2012, hereafter N12), even if there are indications that most halo encounters are on orbits close to parabolic (see e.g. Khochfar & Burkert 2006). In this section we attempt to study the effect of orbital energy using the data of our simulation.

If we know the orbital energy, we can predict analytically the merger-driven evolution of the virial velocity dispersion σ_V: the dissipationless merging of two virialized systems, which have kinetic energies, respectively, $T_1 = M_1\sigma_{V,1}^2/2$ and $T_2 = M_2\sigma_{V,2}^2/2$, on a barycentric orbit of energy E_{orb}, results in a system that, when in equilibrium, has virial velocity dispersion (see Nipoti et al. 2003)

$$\sigma_{V,f}^2 = \frac{M_1\sigma_{V,1}^2 + M_2\sigma_{V,2}^2}{M_1 + M_2} - 2\frac{E_{\mathrm{orb}}}{M_1 + M_2}, \qquad (15)$$

assuming no mass-loss (the subscript f indicates the final value). As long as $\sigma_0 \propto \sigma_V$ (see Section 2.3), equation (15) can be used to predict also the evolution of σ_0.

Similarly, one can predict how the size of the halo is evolving in the merging process: assuming a linear proportionality $r_h \propto r_g$ (see Section 3.2 and Fig. 2), we have that $r_h \propto M/\sigma_V^2$. We can use equation (15) to make predictions in the context of a simple dry merging model: we calculate the half-mass radius of the halo at a given redshift, then we predict its evolution calculating the ratio

$$\frac{r_{h,f}}{r_{h,1}} = \frac{M_1 + M_2}{M_1}\frac{\sigma_{V,1}^2}{\sigma_{V,f}^2}, \qquad (16)$$

where $\sigma_{V,f}^2$ was calculated through equation (15) and we have taken halo 1 as reference progenitor.

4.2.2 Orbital parameters

To account for the contribution of E_{orb} in the evolution of σ_0 and r_h for our haloes (i.e. to apply equation 15), we need to extract the merger orbital parameters from our simulation. We have reconstructed the merger histories of the haloes and then calculated the orbital parameters of the encounters in the point-mass approximation (hereafter PMA) of the progenitors (i.e. approximating every merging halo as a point located in its centre of mass and having the same mass as the object; see e.g. Khochfar & Burkert 2006; Wetzel 2011).

As well known, the orbit of a collision is completely characterized by two parameters, for instance the orbital energy and the orbital angular momentum or the eccentricity and the pericentric radius. Here we find convenient to characterize the orbits of our mergers with the orbital energy E_{orb} and the eccentricity

$$e = \sqrt{1 + \frac{2E_{\mathrm{orb}}L_{\mathrm{orb}}^2}{\mu(GM_1M_2)^2}}, \qquad (17)$$

where M_1 and M_2 are the masses of the two colliding systems, L_{orb} is the norm of the barycentric orbital angular momentum and $\mu \equiv M_1M_2/(M_1 + M_2)$ is the reduced mass. In Fig. 7 we plot the histograms of E_{orb} and e (computed in the PMA) of the encounters experienced by a $M(z=0) \simeq 5.5 \times 10^{14}\,\mathrm{M_\odot}$ DM halo in our simulation from $z \simeq 2.5$ to 0. We find that the distribution of the orbital energies has a clear peak at $E_{\mathrm{orb}} \simeq 0$ (left-hand panel of Fig. 7) and that of the eccentricities have a clear peak at $e \simeq 1$ (right-hand panel of Fig. 7), with both distributions having non-negligible tails both at bound orbits ($e < 1$ and $E_{\mathrm{orb}} < 0$) and unbound orbits ($e > 1$ and $E_{\mathrm{orb}} > 0$). Overall, our findings are in agreement with those of Khochfar & Burkert (2006): the large majority of the mergers happen on orbits close to parabolic.

The orbital potential energy computed in the PMA ($U_{\mathrm{orb,\,PMA}}$) is always larger (in modulus) than the actual orbital potential energy U_{orb}, computed for the extended objects. As an example, one can think of a toy model in which the two particle systems are initially very far away, where the PMA is justified, and then they start to get nearer and nearer up to the limit in which the centres of mass of the two system coincide: in this limit the orbital potential U_{orb} in the PMA diverges, while that of the extended system is still finite.

We tried to obtain a better estimate of the orbital energy by empirically correcting $U_{\mathrm{orb,\,PMA}}$ as follows. We computed the relative distance d_{rel} of a merger as the distance of the centres of the haloes in the snapshot before the merging, i.e. it is the latest snapshot in which the two haloes are distinct. Calculating the distribution of d_{rel} of the collisions in our simulation, we find that it peaks at $d_{\mathrm{rel}} \simeq r_\Delta$
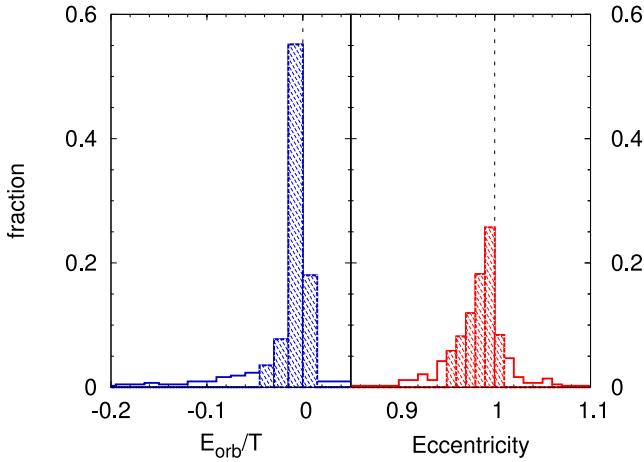
Figure 7. Histograms of the orbital energies (left-hand panel) and of the eccentricities (right-hand panel), computed in the PMA, of the mergers experienced by a $M(z=0) \simeq 5.5 \times 10^{14}\,M_\odot$ DM halo, from $z \simeq 2.5$ to 0. The orbital energies are normalized to the internal energy $T = M\sigma_V^2/2$ of the reference halo. The dashed area, centred on the median value, contains 80 per cent of the counts.

of the biggest merging halo. Assuming an NFW (see Navarro, Frenk & White 1997) profile for the dark haloes, we made some experiments in order to evaluate the overestimate of $|U_{orb}|$ in the PMA varying the parameters of the haloes (such as mass ratio, size ratio and concentration) and, most important, the relative distance between their centres of mass. We used GADGET-2 to calculate the U_{orb} of the encounter between the two systems and we compared it to that calculated in the PMA. We find that, quite independently of the structural parameters of the haloes, in a range of relative distances consistent with that measured in our simulation, $U_{orb} \simeq U_{orb,\,PMA}/2$.

4.2.3 Application to N-body data

In the hypothesis that mergers are the driving mechanism for halo evolution, it is possible, with equation (15), to predict the evolutionary track of a halo in the $M-\sigma_0$ plane across different snapshots in the simulation. For a given halo, starting from M and σ_0 of the most massive progenitor, we considered one at a time every merger in the halo merger tree and we used for each of them equation (15) to predict the evolution of σ_0 after the collisions. In Fig. 8 (top panel) we show the evolution of a representative halo in the σ_0-M plane and we compare it with the predictions of three dry-merging models based on equation (15): the parabolic-merger model (i.e. $E_{orb} = 0$), the PMA model ($E_{orb} = E_{orb,\,PMA}$, where $E_{orb,\,PMA}$ is the orbital energy computed in the PMA) and the corrected PMA model ($U_{orb} = U_{orb,\,PMA}/2$; see Section 4.2.2). The relative errors of the models with respect to the N-body data (bottom panel of Fig. 8) indicate that in the majority of the cases, the parabolic merger approximation tends to underestimate the σ_0 evolution by a factor of ≈ 20–30 per cent, while $E_{orb} = E_{orb,\,PMA}$ model tends to overestimate its growth up to ≈ 80 per cent, probably due to the overestimate of $|U_{orb}|$ introduced by the PMA. When we apply the empirical correction we find a much better agreement with the N-body data. We have checked that the resulting behaviour is fairly independent of the halo considered (i.e. on the halo mass at $z \sim 0$).

Using equation (16), where we compute $\sigma_{V,\,f}$ as in equation (15), we are able to predict also the evolution in size of the halo. The results are summarized in Fig. 9. The parabolic merging model

always tends to overestimate the actual size growth of the halo: such trend is in agreement with the analytical expectation of strong growth of the halo size (see Section 4.2.1). On the other hand, the $E_{orb} = E_{orb,\,PMA}$ model is underestimating the r_h evolution. Applying the empirical correction to the orbital energy in the PMA, we find a much better representation of the N-body data with respect to previous cases (see the bottom panel of Fig. 9), in agreement with our previous results on the velocity dispersion evolution (see Fig. 8).

The results above deserve a further comment: since in the code we are using energy is conserved (see Springel 2005), in principle, if we took into account all the possible complications to the merging model we would reproduce the actual measured evolution. Here we focus on the effect of one of these possible complications, namely the orbital energy. Other authors have used this approach before, studying for example the effect of escapers (see e.g. Nipoti et al. 2003; Hilz et al. 2012): in particular, Hilz et al. (2012) found that mass-loss can be very important in reproducing the size growth of collisionless systems in binary mergers simulations. Our effort is complementary to such works: we added a detailed study of the importance of the orbital energy, finding that taking into account such effect in a simple dry merging model can be *crucial* in order to reproduce the halo evolution in a cosmological context.

5 IMPLICATIONS FOR THE SIZE EVOLUTION OF EARLY-TYPE GALAXIES

In the previous sections we have described the evolution in size and velocity dispersion of the population of DM haloes. This evolution is qualitatively similar to that of the observed population of ETGs. The aim of this section is to compare quantitatively our N-body data to observations. Since there are no baryons in the simulation, we need to populate our DM haloes with galaxies, by assigning the stellar mass M_* and the stellar effective radius R_e, which can be done using currently available prescriptions for the stellar-to-halo mass relation (SHMR) and the stellar-to-halo size relation (SHSR).

5.1 The stellar-to-halo mass relation

A critical point in this work is the assignment of stellar masses to the dark haloes of our N-body simulation. To do so, we need to assume a SHMR, i.e. a function that associates a stellar mass M_* to each given halo mass M at a given redshift z. Many prescriptions are available at the time of this writing for this function (see e.g. Behroozi, Conroy & Wechsler 2010; Wake et al. 2011; Leauthaud et al. 2012; Moster, Naab & White 2013), but the detailed properties of the SHMR are still uncertain and debated.

In order to account for the uncertainties in the SHMR, we use two different models of SHMR: Model 1, adopting the prescription of Behroozi et al. (2010, hereafter B10) and Model 2, adopting the prescription of Leauthaud et al. (2012, hereafter L12). A graphical representation of such models can be found in Fig. 10: the SHMR is plotted in different colours in the redshift range $0 \leq z \leq 4$. The functional forms and parameters of the two prescriptions used here are summarized in section 3.2.1 of N12. Throughout the paper we adopt a Chabrier (2003) initial mass function. As in N12, for simplicity, we do not take into account the scatter of the SHMR: to each halo we assign an M_* which is the mean value of the distribution.

We consider a subset of the DM halo population presented in Section 2.2. We cut our sample of objects to have a stellar mass $\log M_*/M_\odot \geq 10.5$ and such that no halo exceeds $M \simeq 4 \times 10^{13}\,M_\odot$. The stellar mass lower limit is so that the population
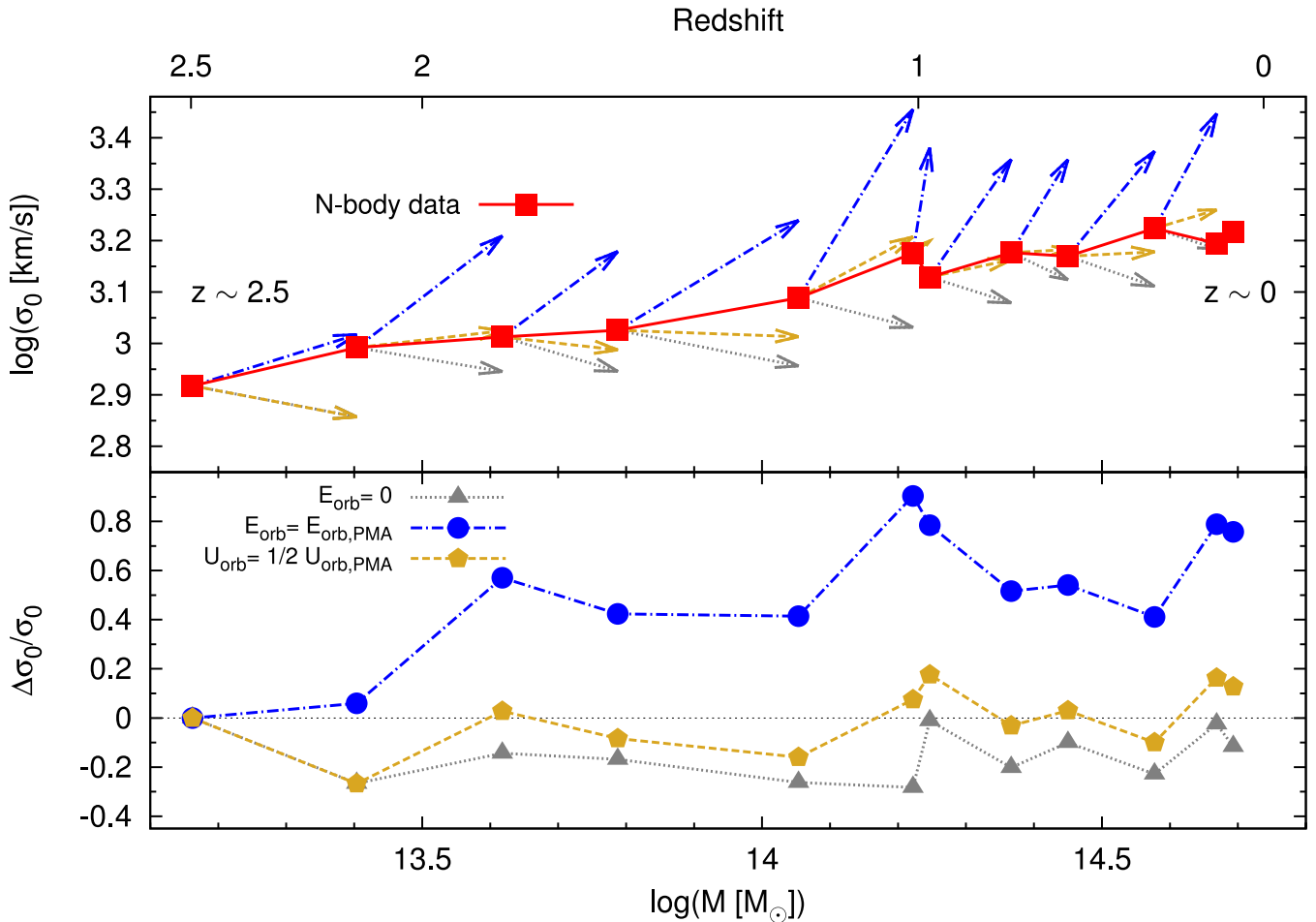
Figure 8. Top panel: evolution of a $M(z = 0) \simeq 5.5 \times 10^{14}$ M$_{\odot}$ halo in the $M-\sigma_0$ plane from $z \simeq 2.5$ to 0 (red filled squares). The different arrows represent the predictions of the σ_0 in the different models, starting from the reference point which is (M, σ_0) of the halo measured at the previous snapshot: grey dotted arrows are in the parabolic ($E_{orb} = 0$) model, the blue dot–dashed arrows in the $E_{orb} = E_{orb, PMA}$ model, in which the orbital energy is computed in the PMA, while the golden short-dashed arrows are in the $U_{orb} = U_{orb, PMA}/2$ model, in which the orbital potential energy is half that in the PMA (see the text). Bottom panel: relative deviations of the model predictions from the measured N-body data.

is dominated by ETGs, since at high stellar mass the fraction of ETGs over the total number of galaxies is larger. The halo mass upper limit is motivated by the fact that DM haloes with mass larger than $M = 4 \times 10^{13}$ M$_{\odot}$ are more likely to host groups of galaxies than single ETGs. We notice here that even if the two models have the same upper limit in halo mass, they have a different upper limit in stellar mass, because of the different model of SHMR used: Model 2 has a steeper slope and a higher normalization at the high-mass end, resulting in more massive galaxies associated with the same halo mass with respect to Model 1. The stellar mass ranges used here are: 3.2×10^{10} M$_{\odot} \leq M_* \leq 1.4 \times 10^{11}$ M$_{\odot}$ (corresponding to 8.5×10^{11} M$_{\odot} \leq M \leq 4 \times 10^{14}$ M$_{\odot}$ in halo mass) for Model 1 and 3.2×10^{10} M$_{\odot} \leq M_* \leq 2 \times 10^{11}$ M$_{\odot}$ (corresponding to 9×10^{11} M$_{\odot} \leq M \leq 4 \times 10^{14}$ M$_{\odot}$ in halo mass) for Model 2.

5.2 The stellar-to-halo size relation

After having characterized every DM halo with a stellar mass under the assumption of a SHMR, the second step is to assign a size, namely an effective radius R_e, to the stellar component. The choice of the SHSR is not trivial and at this time there is not yet a prescription that can be taken as a reference.

However, recently Kravtsov (2013, following the theoretical work of Mo et al. 1998; Fall & Efstathiou 1980) argued that such relation can be measured over a wide range of stellar masses, using abundance matching techniques to derive a functional form. Kravtsov (2013) finds that the relation between the virial radius r_{Δ} of the host halo and the effective radius R_e of the galaxy is linear. Such result confirms the theoretical predictions (see Mo et al. 1998) that the virial radius of the halo is linearly proportional to the size of the galactic disc and that the constant of proportionality depends on the spin parameter $\lambda = J|E|^{1/2}G^{-1}M^{-5/2}$, where J is the norm of the angular momentum of the halo, E is the total energy of the halo and G is the gravitational constant. Moreover, the fact that both early-type and late-type galaxies follow this linear SHSR with a scatter of $\sim$20 per cent (see Kravtsov 2013) can be interpreted as the fact that the Mo et al. (1998) model not only works for disc galaxies, but it also represents a general behaviour of all types of massive galaxies.

Here we assume $R_e \propto r_h$, where r_h is the halo half-mass radius, defined in Section 2.2. However, in Section 2.3 we showed that $r_h \propto r_{\Delta}$, on average, so our assumption is consistent with the results of Kravtsov (2013). As a check to this hypothesis, we compare the stellar mass–effective radius correlation for our model galaxies (i.e. M_*-R_e) at $z = 0$ with that observed in the local Universe,
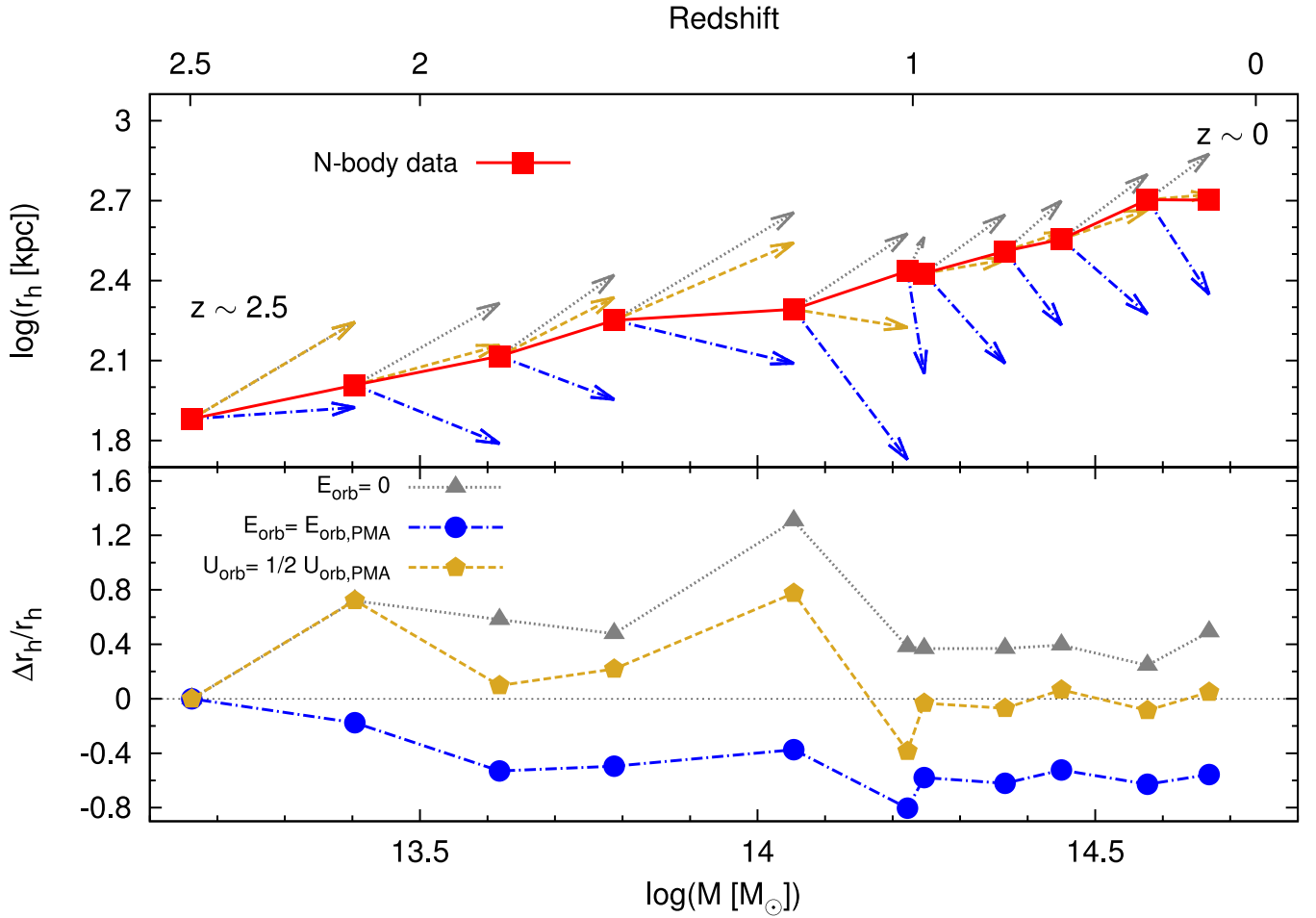
Figure 9. Same as Fig. 8, but for the evolution in the $M-r_h$ plane.
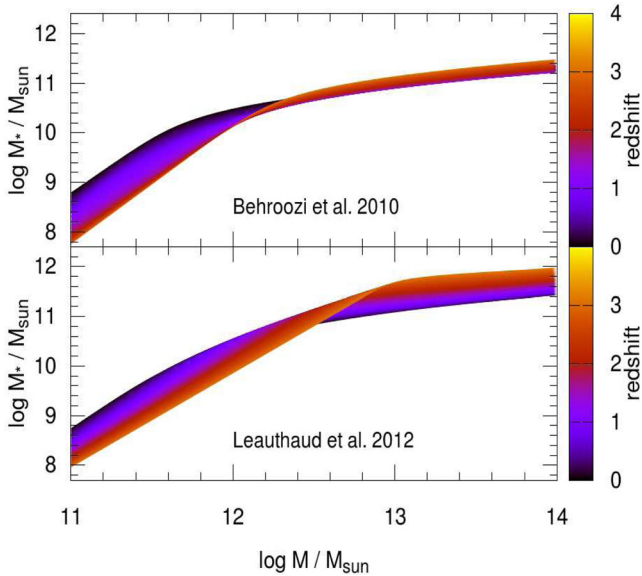

Figure 10. Stellar mass M_* as a function of the halo mass M and redshift according to the prescriptions of B10 (top panel; here used in Model 1) and L12 (bottom panel; here used in Model 2).
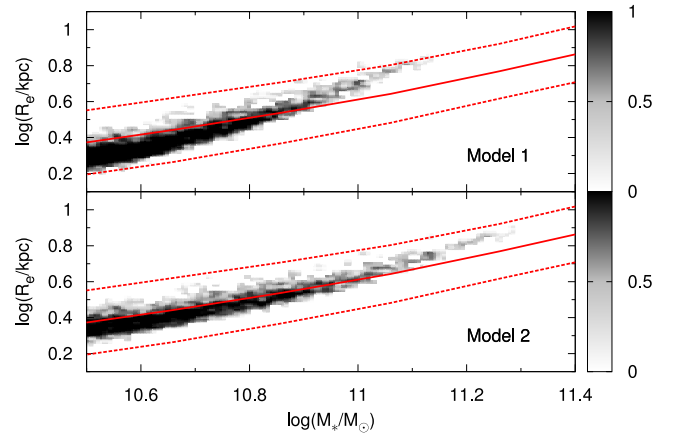

Figure 11. Distribution in the plane stellar mass–effective radius of the sample of model galaxies obtained by populating the $z \simeq 0$ simulated DM haloes according to Model 1 (top panel) and Model 2 (bottom panel). In both panels, the grey-scale is proportional to the logarithm of the number counts of haloes in the binned plane and the solid line is the best-fitting relation of Shen et al. (2003), for SDSS galaxies, with the corresponding 1σ scatter (dashed lines).

taking as reference the M_*-R_e correlation of the ETGs in the Sloan Digital Sky Survey (SDSS; Shen et al. 2003). In Fig. 11 we plot the distribution of the effective radius as a function of the stellar mass for our model galaxies in Models 1 and 2 (see Section 5.1), and we
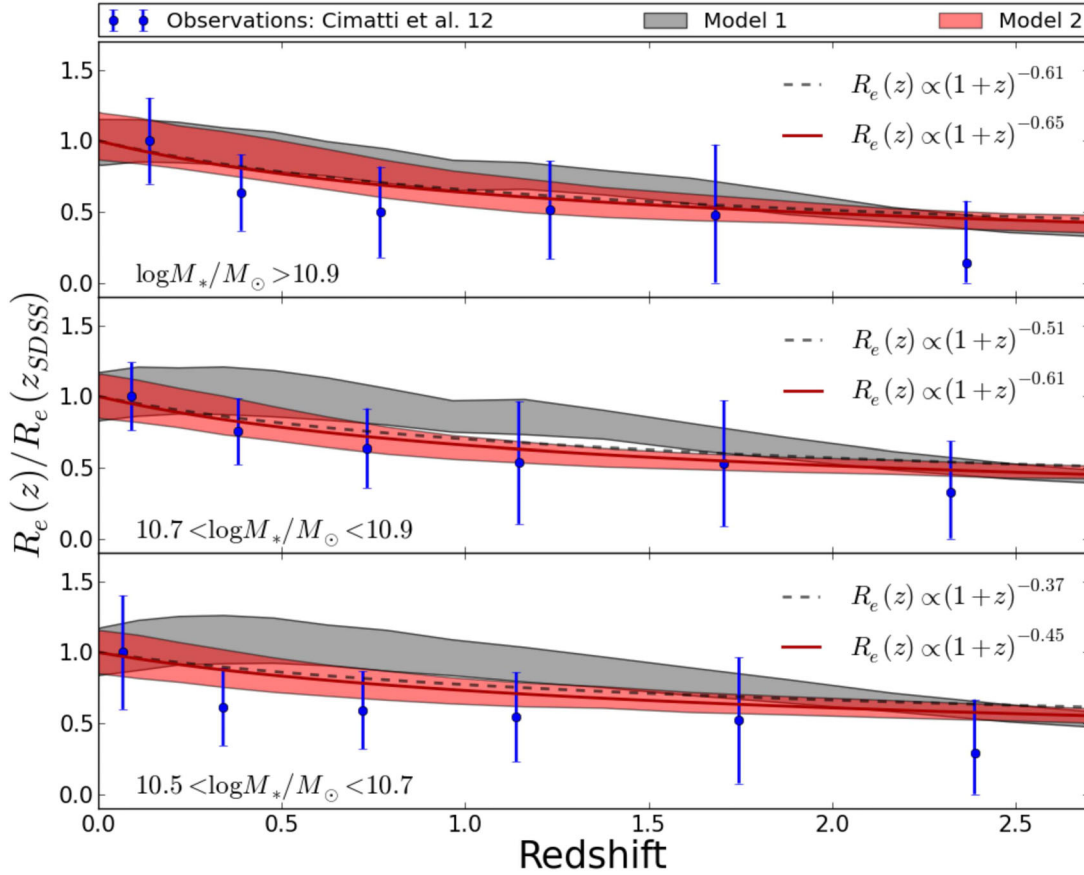
Figure 12. Average effective radius R_e as a function of redshift for simulated galaxies of Model 1 (grey bands) and Model 2 (red bands) of this work and for observed ETGs of CNC12 (blue filled circles). Overplotted are also the best-fitting power laws $R_e \propto (1 + z)^\gamma$ to Model 1 (grey dashed line) and Model 2 (red solid line). Each panel refers to the indicated stellar mass interval and the radii are normalized to the average R_e of SDSS galaxies in that mass interval. The models are anchored to the lowest-z (i.e. SDSS) observational points (see the text). The vertical bars and the widths of the bands indicate one standard deviation.

compare it to the best-fitting relation of Shen et al. (2003). In particular, we have used $R_e/r_h = 0.031$ for Model 1 and $R_e/r_h = 0.042$ for Model 2, which are in reasonable agreement with the expectations of Mo et al. (1998) and the results of Kravtsov (2013), given that on average we find $r_h/r_\Delta \simeq 0.82$ in the simulated haloes. Overall, Fig. 11 shows that the distribution of the $z \simeq 0$ model galaxies in the $R_e - M_*$ plane is consistent with that of SDSS galaxies. In more detail, Model 2, with a best-fitting $R_e \propto M_*^{0.64}$, appears to reproduce better the SDSS data (best-fitting $R_e \propto M_*^{0.56}$) than Model 1 (best-fitting $R_e \propto M_*^{0.84}$).

When comparing our models to observations (see Section 5.3) we will assume that the ratio R_e/r_h is independent of M and z. We will study only the redshift evolution of size ratios [namely, $R_e(z)$ normalized to $R_e(z \simeq 0)$], so the results are independent of the actual value of R_e/r_h. We note that an underlying assumption of our models is that baryons do not affect substantially the structural evolution of DM haloes. The stellar and DM components are expected to affect each other significantly, even in dissipationless mergers (see e.g. Hilz et al. 2013). However, our results are not sensitive to this effect as long as it is independent on halo mass.

5.3 Size evolution of early-type galaxies: comparing models with observations

Here we compare the size evolution of our model galaxy sample (built from the *N*-body data as described in Sections 5.1 and 5.2)

with that of the observed population of ETGs. In particular, we take as reference observational sample the collection of ETGs in the redshift range $0 \lesssim z \lesssim 3$ presented by Cimatti, Nipoti & Cassata (2012, hereafter CNC12). We show such comparison in Fig. 12: we compute the average size of the model galaxy sample at different times (16 snapshots of the *N*-body simulation in the range $0 \leq z \leq 3$) and we normalize it to that at the mean redshift of the SDSS. Following CNC12, we plot the evolution in three different mass bins. In Fig. 12 we are showing a sort of *backward* evolution: we are normalizing our models to be in agreement with the data at $z \simeq 0$ and we follow the evolution of the average size of the model galaxies at higher redshift. Our choice is motivated by the fact that we anchor the models to observations in the local Universe, which are more numerous with respect to $z \simeq 2.5-3$ data.

The distribution of our model galaxies significantly overlaps with that of the observed ETGs of CNC12, but the models suffer from a systematic underestimate of the size growth in all the mass bins, in particular at $z > 2$. At $z < 2$ the models (especially Model 2, which is based on L12) are consistent within the scatter with the observational data, suggesting that the host haloes actually left their footprint in the stellar density at the time of galaxy quenching and that the after-quenching evolution of the galaxies mimicked that of the haloes. To give reference numbers, for both models, we computed the ratio $R_e(z \simeq 2.5)/R_e(z \simeq 0)$ in the three different mass bins finding that from $z \simeq 2.5$ to 0 the average effective radius increases by a factor of ≈ 2 in the lowest mass bin ($\log M_*/M_\odot < 10.7$) and

Table 1. Summary of the best-fitting power laws $R_e(z) \propto (1+z)^\gamma$ and $\sigma_*(z) \propto (1+z)^\delta$ to our models in the range $0 \lesssim z \lesssim 2.5$, for different stellar mass bins (see Sections 5.3 and 5.4).

Stellar mass	Model 1		Model 2	
	γ	δ	γ	δ
$\log M_*/M_\odot > 10.9$	-0.61 ± 0.07	0.28 ± 0.05	-0.65 ± 0.09	0.43 ± 0.07
$10.7 < \log M_*/M_\odot < 10.9$	-0.51 ± 0.06	0.18 ± 0.05	-0.61 ± 0.06	0.20 ± 0.06
$10.5 < \log M_*/M_\odot < 10.7$	-0.37 ± 0.06	0.04 ± 0.05	-0.45 ± 0.06	0.01 ± 0.05

by a factor of ≈ 3 in the highest one ($\log M_*/M_\odot > 10.9$). For comparison, most observational data agree on an evolution of the average effective radius of the ETG population of a factor of $2-5$ from $z \gtrsim 2$ to the present (see e.g. CNC12).

In Table 1 we report the best-fitting values of γ, where $R_e \propto (1+z)^\gamma$, for both models in the range $0 \lesssim z \lesssim 2.5$ and in the three mass bins. We find values of γ similar to those in CNC12 when they exclude the $z > 2$ data, while the models fail at reproducing the observed slopes which take into account also the higher redshift points.

Our analysis shows that, provided that the galaxy formation process produces a linear SHSR, the observed size evolution of the population of ETGs up to $z \simeq 2$ could be explained by the underlying size evolution of the halo population, in the sense that quiescent galaxies mimic the host halo evolution. At $z > 2$ the average size of the observed population of ETGs evolves significantly faster than predicted by our simple models (in agreement with CNC12; N12). This difference at $z \gtrsim 2$ can possibly give us some insights into the role dissipative effects, such as star formation or active galactic nuclei (AGN) feedback: it might not be a mere coincidence that at $z \approx 2$ there are the peaks of the cosmic star formation rate (Lilly et al. 1996; Madau et al. 1996) and of AGN activity (see e.g. Merloni & Heinz 2008; Gruppioni et al. 2011).

Overall, our results are in agreement with those of previous investigations (CNC12; Newman et al. 2012; N12), which are in a sense complementary to this work. For instance, we note that the approach used here is different from that of CNC12, who (following N12) treat in their model only the evolution of individual galaxies and do not include the contribution of galaxies that have become quiescent at relatively low redshift. In other words, when comparing models to observations, CNC12 do not try to account for the so-called progenitor bias (see e.g. Saglia et al. 2010; Carollo et al. 2013) because they assume that the observed population of high-z ETGs is representative of the progenitors of present-day ETGs. Our approach, though simple, should be more robust against the progenitor bias: in our sample of simulated objects, at any redshift, we can have in principle both galaxies that have just stopped forming stars (and that are identified for the first time as ETGs) and galaxies that became quiescent much earlier. However, it must be stressed that our model is limited by the fact that we are assuming that galaxies grow in size and mass so that the SHMR and SHSR are reproduced at all redshifts, without having specified any underlying physical model for such growth. In this respect, a more physically justified approach is that of CNC12 and N12, who assume that the size and mass growth of ETGs is driven by dry mergers, finding that, under this hypothesis, the SHMR inferred from observations is not necessarily reproduced (see N12). In summary, our results, combined with those of similar previous works, suggest a scenario in which, at least up to $z \simeq 2$, the observed growth of ETGs reflects the underlying growth of their host DM haloes.

5.4 Velocity dispersion evolution of early-type galaxies: comparing models with observations

In this section we compare the stellar velocity dispersion evolution of our model ETGs with that observed up to $z \simeq 2$. For such comparison we rely on the data collection of ETGs from Belli, Newman & Ellis (2014) and van de Sande et al. (2013). We use a very simple recipe to get the stellar velocity dispersion of the model galaxies: consistent with our choice for the assignment of R_e (i.e. $R_e \propto r_h$), we assume a scaling with the halo properties of the form $\sigma_*^2 \propto M_*(M)/R_e(r_h)$, where we use the SHMR (Section 5.1) and SHSR (Section 5.2) from Model 1 and 2.

We check this recipe for ETGs at $z \simeq 0$: in Fig. 13 it is plotted the stellar mass–velocity dispersion relation at $z \simeq 0$ for our model ETGs which we compare to SDSS observations data from Hyde & Bernardi (2009). Overall, both models are able to represent fairly well the SDSS data within their uncertainties. However, we notice that Model 2 works systematically better than Model 1 in reproducing the observed $M_*-\sigma_*$: Model 1 is best fitted by $\sigma_* \propto M_*^{0.11}$, while for Model 2 we find $\sigma_* \propto M_*^{0.2}$, closer to the Hyde & Bernardi (2009) relation $\sigma_* \propto M_*^{0.286}$.

Fig. 14 shows the average velocity dispersion (*backward*) evolution of our model galaxies in the redshift range $0 \lesssim z \lesssim 2$. We compute the average σ_* as a function of redshift, we anchor the data from Belli et al. (2014) and van de Sande et al. (2013) to a reference value for the local Universe taken from Hyde & Bernardi (2009) and we directly compare the backward evolution with data available for individual ETGs. Qualitatively we find a reasonable agreement with observations of high-mass (i.e. $\log M_*/M_\odot > 10.9$) passive galaxies up to $z \simeq 2$. The predictions, especially those of Model 2, are able to reproduce the evolutionary trend in the observations, even though
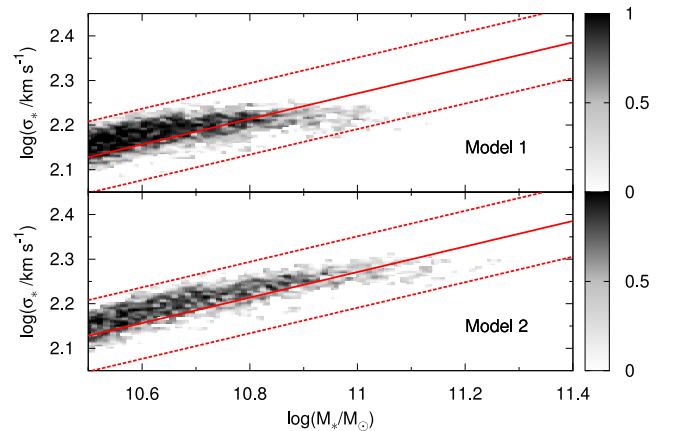

Figure 13. Same as Fig. 11, but in the stellar mass–velocity dispersion plane. In both panels, the solid line is the best-fitting relation of Hyde & Bernardi (2009), for SDSS galaxies, with the corresponding 1σ scatter (dashed lines).
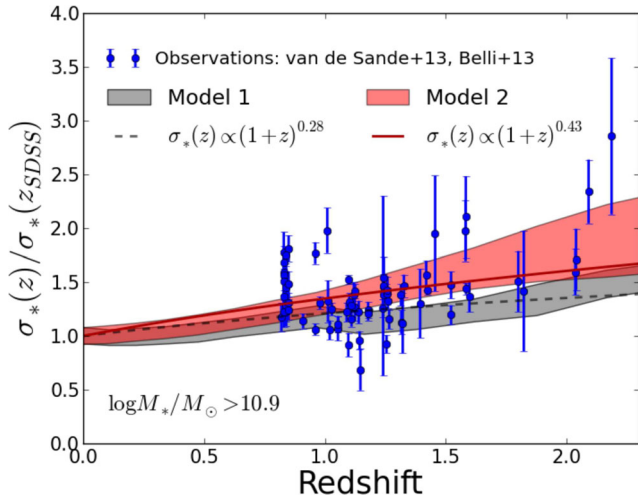
Figure 14. Average velocity dispersion σ_* as a function of redshift for simulated galaxies of Model 1 (grey bands) and Model 2 (red bands) of this work and for observed ETGs of van de Sande et al. (2013) and Belli et al. (2014, blue filled circles). Here we restrict to stellar masses $\log M_*/M_\odot >$ 10.9. Overplotted are also the best-fitting power laws $\sigma_* \propto (1+z)^\delta$ (grey dashed line and red solid line, respectively, to Model 1 and Model 2). The models are anchored to the lowest-z (i.e. SDSS) observational points (see the text), as in Fig. 12. The vertical bars and the widths of the bands indicate one standard deviation.

there is significant scatter. Quantitatively, we find that Model 2 evolution is well fitted by $\sigma_* \propto (1+z)^\delta$, with $\delta = 0.43 \pm 0.07$, while for Model 1 we find $\delta = 0.28 \pm 0.05$. For comparison, fitting the individual observations with a similar power-law evolution gives us $\delta = 0.36 \pm 0.02$, which is consistent within the uncertainties at least with Model 2. The model galaxies have decreased on average their velocity dispersion by a factor of $\sigma_*(z \simeq 2)/\sigma_*(z \simeq 0) \approx 1.4{-}1.8$; for comparison van de Sande et al. (2013) quote an evolution in their sample of data of a factor of $\approx 1.4 - 1.7$.

In Table 1 we summarize the results of fitting the velocity dispersion evolution in both models with simple power laws, in the range $0 \lesssim z \lesssim 2.5$ and in the three stellar mass bins considered in Section 5. The numbers reported in Table 1 and the trends shown by Figs 12 and 14 are also in good agreement with previous results of the *average* size and velocity dispersion evolution of stellar systems in hydrodynamical cosmological simulations (see e.g. Oser et al. 2012).

The above results on the velocity–dispersion evolution depend on the assumed assignment of σ_* to haloes (i.e. $\sigma_*^2 \propto M_*/R_e$). A different choice could be $\sigma_* \propto \sigma_0$ (where σ_0 is the halo velocity dispersion); however, we have verified that assuming a scaling of that type leads to a very poor comparison of the $M_*{-}\sigma_*$ relation with data for the local Universe. This suggests that the evolution of the velocity dispersion of the stellar component is somewhat decoupled from that of the dark component: while σ_0 increases with time for individual haloes in our sample (see Fig. 6), vice versa σ_* of individual model galaxies tends to decrease as a function of time, if one assumes $\sigma_*^2 \propto M_*/R_e$.

The same trend of velocity dispersion decreasing with time for individual galaxies is found in the cosmological hydrodynamical simulations of Oser et al. (2012) and Oser (private communication). However, it must be noted that Dubois et al. (2013), who also studied the evolution of ETGs using cosmological hydrodynamical simulations, found that the velocity dispersion of individual galaxies increases with time.

6 SUMMARY AND CONCLUSIONS

Motivated by the observational finding that ETGs are, on average, more compact at higher redshift, we have explored the hypothesis that such evolution is mainly driven by the systematic redshift dependence of the structural properties of their host DM haloes. Using a cosmological N-body simulation, we have followed the evolution of the structural and kinematical properties of a DM halo population in the ΛCDM framework, focusing on the halo mass range $10^{11} \lesssim M/M_\odot \lesssim 5 \times 10^{14}$. Starting from a sample of simulated haloes, we have built a sample of model ETGs and we have compared the redshift evolution of their sizes with that of observed galaxies.

The main results can be summarized as follows.

(i) At $z = 0$ the haloes are well represented by $\sigma_0 \propto M^{0.329 \pm 0.001}$ and $r_h \propto M^{0.320 \pm 0.002}$ at $z = 0$, where r_h is the half-mass radius and σ_0 is the central velocity dispersion. These global correlations are remarkably similar to those predicted for the virial quantities of the haloes (namely, $M \propto \sigma_V^3$ and $M \propto r_\Delta^3$), meaning that there is no significant non-homology in the halo population.

(ii) The slopes of the $M{-}\sigma_0$ and $M{-}r_h$ correlations depend only slightly on z, but their normalizations evolve significantly with z in the sense that, at fixed mass, higher-z haloes have smaller r_h and higher σ_0. For instance, at fixed $M = 10^{12}\,M_\odot$ we find $\sigma_0 \propto (1+z)^{0.35}$ and $r_h \propto (1+z)^{-0.71}$.

(iii) The redshift evolution of the halo scaling laws is driven by individual haloes growing in mass following evolutionary tracks $\sigma_0 \propto M^{0.2}$ and $r_h \propto M^{0.6}$. So, while individual haloes grow in mass, their velocity dispersions increase slowly and their sizes grow rapidly.

(iv) The size and velocity dispersion evolution of individual haloes is successfully described by simple dissipationless merging models, in which a key ingredient is the (typically negative) orbital energy of the encounters.

(v) We compare our N-body data with observations of ETGs in the redshift range $0 \lesssim z \lesssim 3$, by populating the DM haloes with galaxies assigning to each halo a stellar mass, an effective radius and a stellar velocity dispersion. We find that the size and velocity dispersion evolution of our model galaxies is in reasonable agreement with the evolution observed for ETGs at least up to $z \simeq 2$. At $z > 2$ the observed size growth is stronger than predicted by our simple models.

The above findings suggest a scenario in which the size and velocity dispersion scaling laws of ETGs derive from underlying scaling laws of the DM haloes. Overall, the results of this work give further support to the idea of a halo-driven evolution of ETGs: galaxy structural and dynamical properties are related to that of their haloes at the time of quenching and the further ETG evolution mimics that of haloes. Of course, the present approach is limited by the fact that we do not include a self-consistent treatment of baryonic physics. In a forthcoming study, we plan to investigate this problem by adding the baryonic evolution in the simulations.

REFERENCES

Behroozi P. S., Conroy C., Wechsler R. H., 2010, ApJ, 717, 379 (B10)
Belli S., Newman A. B., Ellis R. S., 2014, ApJ, 783, 117
Bertschinger E., 2001, ApJS, 137, 1
Binney J., Tremaine S., 2008, Galactic Dynamics, 2nd edn. Princeton Univ. Press, Princeton, NJ
Boylan-Kolchin M., Ma C.-P., Quataert E., 2005, MNRAS, 362, 184
Bryan G. L., Norman M. L., 1998, ApJ, 495, 80
Carollo C. M. et al., 2013, ApJ, 773, 112
Cassata P. et al., 2011, ApJ, 743, 96
Chabrier G., 2003, PASP, 115, 763
Cimatti A. et al., 2008, A&A, 482, 21
Cimatti A., Nipoti C., Cassata P., 2012, MNRAS, 422, L62 (CNC12)
Ciotti L., 1991, A&A, 249, 99
Ciotti L., 2009, Riv. Nuovo Cimento, 32, 1
Daddi E. et al., 2005, ApJ, 626, 680
Damjanov I. et al., 2011, ApJ, 739, L44
Davis M., Efstathiou G., Frenk C. S., White S. D. M., 1985, ApJ, 292, 371
Diemer B., More S., Kravtsov A. V., 2013a, ApJ, 766, 25
Diemer B., Kravtsov A. V., More S., 2013b, ApJ, 779, 159
Djorgovski S., Davis M., 1987, ApJ, 313, 59
Dressler A., Lynden-Bell D., Burstein D., Davies R. L., Faber S. M., Terlevich R., Wegner G., 1987, ApJ, 313, 42
Dubois Y., Gavazzi R., Peirani S., Silk J., 2013, MNRAS, 433, 3297
Efstathiou G., Davis M., White S. D. M., Frenk C. S., 1985, ApJS, 57, 241
Evrard A. E. et al., 2008, ApJ, 672, 122
Faber S. M., Jackson R. E., 1976, ApJ, 204, 668
Fakhouri O., Ma C.-P., Boylan-Kolchin M., 2010, MNRAS, 406, 2267
Fall S. M., Efstathiou G., 1980, MNRAS, 193, 189
Fan L., Lapi A., De Zotti G., Danese L., 2008, ApJ, 689, L101
Fan L., Lapi A., Bressan A., Bernardi M., De Zotti G., Danese L., 2010, ApJ, 718, 1460
Ferguson H. C. et al., 2004, ApJ, 600, L107
Ferrarese L., Merritt D., 2000, ApJ, 539, L9
Gebhardt K. et al., 2000, ApJ, 539, L13
Graham A. W., Driver S. P., 2007, ApJ, 655, 77
Graham A. W., Erwin P., Caon N., Trujillo I., 2001, ApJ, 563, L11
Gruppioni C., Pozzi F., Zamorani G., Vignali C., 2011, MNRAS, 416, 70
Hilz M., Naab T., Ostriker J. P., Thomas J., Burkert A., Jesseit R., 2012, MNRAS, 425, 3119
Hilz M., Naab T., Ostriker J. P., 2013, MNRAS, 429, 2924
Hopkins P. F., Lauer T. R., Cox T. J., Hernquist L., Kormendy J., 2009a, ApJS, 181, 486
Hopkins P. F., Bundy K., Murray N., Quataert E., Lauer T. R., Ma C.-P., 2009b, MNRAS, 398, 898
Hopkins P. F., Narayanan D., Murray N., 2013, MNRAS, 432, 2647
Hyde J. B., Bernardi M., 2009, MNRAS, 394, 1978
Ishibashi W., Fabian A. C., Canning R. E. A., 2013, MNRAS, 431, 2350
Kereš D., Vogelsberger M., Sijacki D., Springel V., Hernquist L., 2012, MNRAS, 425, 2027

Khochfar S., Burkert A., 2006, A&A, 445, 403
Khochfar S., Silk J., 2006, ApJ, 648, L21
Knebe A. et al., 2011, MNRAS, 415, 2293
Knollmann S. R., Knebe A., 2009, ApJS, 182, 608
Kormendy J., 1977, ApJ, 218, 333
Kravtsov A. V., 2013, ApJ, 764, L31
Krogager J.-K., Zirm A. W., Toft S., Man A., Brammer G., 2013, preprint (arXiv:1309.6316)
Lacey C., Cole S., 1993, MNRAS, 262, 627
Lanzoni B., Ciotti L., Cappi A., Tormen G., Zamorani G., 2004, ApJ, 600, 640
Laporte C. F. P., White S. D. M., Naab T., Gao L., 2013, MNRAS, 435, 901
Lau E. T., Nagai D., Kravtsov A. V., 2010, ApJ, 708, 1419
Leauthaud A. et al., 2012, ApJ, 744, 159 (L12)
Lilly S. J., Le Fevre O., Hammer F., Crampton D., 1996, ApJ, 460, L1
López-Sanjuan C. et al., 2012, A&A, 548, A7
Madau P., Ferguson H. C., Dickinson M. E., Giavalisco M., Steidel C. C., Fruchter A., 1996, MNRAS, 283, 1388
Magorrian J. et al., 1998, AJ, 115, 2285
Merloni A., Heinz S., 2008, MNRAS, 388, 1011
Mo H. J., Mao S., White S. D. M., 1998, MNRAS, 295, 319
Moster B. P., Naab T., White S. D. M., 2013, MNRAS, 428, 3121
Munari E., Biviano A., Borgani S., Murante G., Fabjan D., 2013, MNRAS, 430, 2638
Naab T., Johansson P. H., Ostriker J. P., 2009, ApJ, 699, L178
Navarro J. F., Frenk C. S., White S. D. M., 1997, ApJ, 490, 493
Newman A. B., Ellis R. S., Bundy K., Treu T., 2012, ApJ, 746, 162
Nipoti C., Londrillo P., Ciotti L., 2003, MNRAS, 342, 501
Nipoti C., Treu T., Bolton A. S., 2009a, ApJ, 703, 1531
Nipoti C., Treu T., Auger M. W., Bolton A. S., 2009b, ApJ, 706, L86
Nipoti C., Treu T., Leauthaud A., Bundy K., Newman A. B., Auger M. W., 2012, MNRAS, 422, 1714 (N12)
Oser L., Naab T., Ostriker J. P., Johansson P. H., 2012, ApJ, 744, 63
Poggianti B. M., Moretti A., Calvi R., D'Onofrio M., Valentinuzzi T., Fritz J., Renzini A., 2013, ApJ, 777, 125
Power C., Navarro J. F., Jenkins A., Frenk C. S., White S. D. M., Springel V., Stadel J., Quinn T., 2003, MNRAS, 338, 14
Ragone-Figueroa C., Granato G. L., 2011, MNRAS, 414, 3690
Saglia R. P. et al., 2010, A&A, 524, A6
Saracco P., Longhetti M., Andreon S., 2009, MNRAS, 392, 718
Shen S., Mo H. J., White S. D. M., Blanton M. R., Kauffmann G., Voges W., Brinkmann J., Csabai I., 2003, MNRAS, 343, 978
Sonnenfeld A., Nipoti C., Treu T., 2014, ApJ, preprint (arXiv:1310.3280)
Springel V., 2005, MNRAS, 364, 1105
Springel V., Yoshida N., White S. D. M., 2001, New Astron., 6, 79
Stanek R., Rasia E., Evrard A. E., Pearce F., Gazzola L., 2010, ApJ, 715, 1508
Stiavelli M. et al., 1999, A&A, 343, L25
Stringer M. J., Shankar F., Novak G. S., Huertas-Company M., Combes F., Moster B. P., 2013, preprint (arXiv:1310.3823)
Trujillo I. et al., 2006, ApJ, 650, 18
van de Sande J. et al., 2013, ApJ, 771, 85
van der Wel A., Holden B. P., Zirm A. W., Franx M., Rettura A., Illingworth G. D., Ford H. C., 2008, ApJ, 688, 48
van Dokkum P. G. et al., 2008, ApJ, 677, L5
Vogelsberger M., Sijacki D., Kereš D., Springel V., Hernquist L., 2012, MNRAS, 425, 3024
Wake D. A. et al., 2011, ApJ, 728, 46
Wetzel A. R., 2011, MNRAS, 412, 49

This paper has been typeset from a T$_{\rm E}$X/L$^{\rm A}$T$_{\rm E}$X file prepared by the author.